Tunable elastic wave modulation via local phase dispersion measurements of a piezoelectric metasurface with signal correlation enhancement

Cite as: J. Appl. Phys. 133, 244901 (2023); doi: 10.1063/5.0145927 Submitted: 8 February 2023 · Accepted: 3 June 2023 · Published Online: 29 June 2023







Joshua Dupont,¹ 🗓 Ting Wang,¹ 🗓 Richard Christenson,² and Jiong Tang^{1,a)} 🗓

AFFILIATIONS

- Department of Mechanical Engineering, University of Connecticut, Storrs, Connecticut 06269, USA
- ²Department of Civil and Environmental Engineering, University of Connecticut, Storrs, Connecticut 06269, USA

ABSTRACT

Tunable piezoelectric metasurfaces have been proposed as a means of adaptively steering incident elastic waves for various applications in vibration mitigation and control. Bonding piezoelectric material to thin structures introduces electromechanical coupling, enabling structural dynamics to be altered via tunable electric shunts connected across each unit cell. For example, by carefully calibrating the inductive shunts, it is possible to implement the discrete phase shifts necessary for gradient-based waveguiding behaviors. However, experimental validations of localized phase shifting are challenging due to the narrow bandgap of local resonators, resulting in poor transmission of incident waves and high constitutive to transient poice. These factors in combination with the difficulties in experimental circuitry synthesis, can lead to and high sensitivity to transient noise. These factors, in combination with the difficulties in experimental circuitry synthesis, can lead to significant variability of data acquired within the bandgap operating region. This paper presents a systematic approach for extracting & localized phase shifts by taking advantage of the inherent correlation between the incident and transmitted wavefronts. During this procedure, matched filtering greatly reduces noise in the transmitted signal when operating in or near bandgap frequencies. Experimental results demonstrate phase shifts as large as -170° within the locally resonant bandgap, with an average 28% reduction in error relative to a direct time domain measurement of phase, enabling effective comparison of the dispersive behavior with corresponding analytical and finite element models. In addition to demonstrating the tunable waveguide characteristics of a piezoelectric metasurface, this technique can easily be extended to validate localized phase shifting of other elastic waveguiding metasurfaces.

Published under an exclusive license by AIP Publishing. https://doi.org/10.1063/5.0145927

I. INTRODUCTION

The concept of elastic waveguiding refers to the controlled redirection and manipulation of propagating waves in elastic media, which has attracted a great deal of attention across a diverse range of application fields. In the medical field, elastic waveguiding enables ultrahigh resolution for medical diagnosis via ultrasonic imaging, human motion activity monitoring, and sensory waveguided robotics.2 Flexible optical waveguides have also exhibited great potential in the field of wearable, implantable, and optical sensing.³ For structure health monitoring, elastic waveguiding has been investigated for detecting core-skin debonding damage in aluminum honeycomb structures.4 Waveguiding is generally achieved using metamaterials that are engineered to alter the dispersive characteristics of the elastic medium at the local level, permitting the formation of phase shift gradients which are used to modulate and

steer incident wavefronts. Such phase gradient metasurfaces have been applied for enhanced sensing of flexural waves,5 structural vibration isolation, mode localization, and energy harvesting, and

Pioneering research demonstrated the realizability of periodically arranged local resonators and/or Bragg-scattering elements for direct wavefield manipulation. Zhu et al. 11 experimentally measured anomalous refraction of up to 23° using machined geometric tapers tailored to specific local resonances. Cao et al. 12 proposed a metasurface of lead-antimony subunits of varying width embedded in an aluminum plate to realize vertical and oblique shear-wave deflections. Additional structures incorporating porosity, Helmholtz resonators, spring-mass, and cantilever type oscillators represent just a few of the designs proposed. 13 Many researchers have since turned their attention to tunable and

a) Author to whom correspondence should be addressed: jiong.tang@uconn.edu

adaptive structures, enabling online reconfigurability and/or realtime control of waveguiding phenomena. With a handful of notable exceptions, e.g., shape memory alloys, 14,15 piezoresistivity, 16,17 tunable mechanical oscillators, 18,19 and piezoelectric metasurfaces are commonly used for this purpose.

The piezoelectric metasurface utilizes an electromechanical coupling between mechanical strain and electrical charge to locally modify the dispersive characteristics of the host structure. This approach offers a high degree of flexibility in design and implementation, facilitating various shunt configurations,²⁰ spatial grading,^{21,22} non-linear circuitry,²³ and active control of elastic waveguides.²⁴ For example, Hu et al.²⁵ investigated a piezoelectric metamaterial beam with a graded distribution of inductive shunts to realize broadband vibration suppression. This results in multiple bandgaps with neighboring center frequencies such that the overall range of transmission loss is widened. Sugino et al.26 presented an experimentally validated programmable metasurface with a digitally tunable local resonance and bandgap width utilizing synthetic impedance circuits. Li et al.²⁷ proposed a phase gradient elastic reflector using a programmable transfer function to realize simultaneous waveguiding and wave mode conversion. Many investigations have also explored novel methods for enhancing the performance of the piezoelectric unit cell by increasing broadband effectiveness. 21,28 Lin and Tol²⁹ recently proposed an electroelastic metasurface that uses multi-modal LC-shunts to enable simultaneous wave focusing at multiple discrete frequencies. Hu et al.3 examined a locally resonant metamaterial beam with negative capacitance coupling between adjacent cells to increase bandwidth and form additional low and high frequency bandgaps. Zheng et al. 31 utilized a one-way voltage amplifier between adjacent piezoelectric unit cells to facilitate non-reciprocal elastic wave propagation. While novel features and promising performance have been shown, experimental studies on waveguides utilizing phase gradient metasurfaces are still challenging. Within the narrow locally resonant bandgap, poor transmission of incident waves and high sensitivity to transient noise are expected. These factors, in combination with the complex challenges in experimental circuitry synthesis, can lead to significant variability of data acquired within the bandgap operating region.

The present research focuses on the investigation and experimental demonstration of local elastic phase shifting using a piezoelectric metasurface with continuously tunable inductive shunts. Phase modulations are acquired at two distinct frequencies, illustrating the reconfigurability of the metasurface structure. The locally resonant dynamics of each unit cell leads to the formation of a narrow transmission bandgap, within which incident waves are strongly reflected. In this frequency range, the transmitted wavefield may become deeply encased in noise, making it challenging to extract the local phase modulation features experimentally.¹⁸ In addition, the measured phase shifts can be highly sensitive to transients and changes in excitation frequency, resulting in a significant potential for measurement error in this operating region. To meet these challenges, a signal correlation procedure³² is adapted to simultaneously filter noise and acquire phase measurements from the transmitted time domain response. This approach may be used in real-time or post-processing and is capable of accurately determining phase shifts at frequencies near the locally resonant bandgap.

The rest of the paper is organized as follows. First, the dispersive characteristics of the piezoelectric unit cell are analyzed through an analytical model based on the transformation matrix method and a finite element eigenfrequency simulations. The resulting dispersion curves are then used to design a 2D metasurface and implement the anomalous refraction of incident waves. The experimental setup is then described, including the implementation of synthetic inductances and the signal correlation method. Next, the expected localized phase shifting behavior is experimentally validated for two case studies (12 and 14 kHz bandgaps) and compared to analytical and finite element models. Finally, the improvement in the relative error of the signal correlation method over direct peak comparison is discussed. The final section concludes the present work and discusses applications and extensions the method to the ongoing research.

PISPERSION ANALYSIS

To manipulate the phase of elastic wave propagation with a second or secon of the method to the ongoing research.

II. DISPERSION ANALYSIS

metasurface, individual unit cells must be designed to locally alter 🕏 the phase of incident waves. This can be done by varying either the propagation path length or the propagation speed at a local level.¹ Here, we investigate the dispersive characteristics of the piezoelectric unit cell illustrated in Fig. 1, with an applied flexural plane wave traveling along the x-direction. The local unit cell is formed by surface bonding a piezoelectric transducer (PZT) to a metal plate. The PZT introduces electromechanical coupling with the unit cell such that energy is converted from the mechanical strain produced by the elastic waves to the electrical charge on the electrodes. Due to the inherent capacitance of the PZT, connecting an inductance L across its terminals forms an electrical LC-oscillator

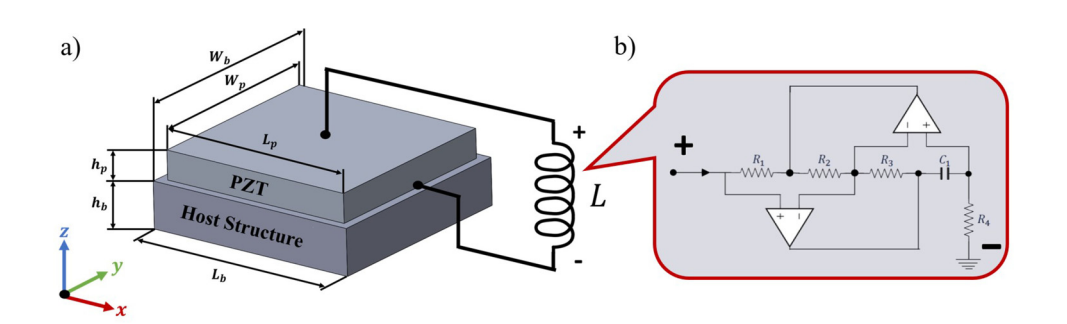


FIG. 1. (a) Unimorph piezoelectric unit cell bonded to a host structure (plate) with an inductive shunt. (b) Semi-active synthetic inductance circuit known as the Antoniou Gyrator used to realize the tunable inductance.

with the local resonance f_L ,³³

$$f_L = \frac{1}{2\pi\sqrt{C_pL}},\tag{1}$$

where C_p is the piezoelectric capacitance. The introduction of this oscillator leads to the formation of a locally resonant bandgap which occurs as the incident wave frequency approaches f_L . With the aid of tunable synthetic inductors, the value of L may be adjusted such that this bandgap occurs near a specified frequency.^{34,35} The circuit illustrated in Fig. 1(b), commonly known as the Antoniou Gyrator, uses operational amplifiers to emulate the electrical impedance of an inductor. Under ideal op-amp assumptions, this circuit leads to a zero real impedance and an effective inductive reactance,3

$$L = \frac{R_1 R_3 R_4}{R_2} C_1, \tag{2}$$

where R_{1-4} and C_1 are resistors and a capacitor corresponding to the circuit diagram in Fig. 1(b). By replacing one of the resistors with a potentiometer, the inductance can be continuously tuned according to Eq. (2). The use of this circuit has three distinct advantages over passive coil inductors for this application; it is tunable, the range of realizable inductances is large, and the resistance is quite low.

The inclusion of tunable synthetic inductors enables control of the dispersive characteristics of the unit cell. The transformation matrix method is used to obtain the dispersion relation of the unit cell while varying inductance. 36,37 The unit cell is simplified into an equivalent two-dimensional structure, considering wave propagation in the \hat{x} direction only. Since the aspect ratio (length to thickness) is less than 10, the Timoshenko beam theory is used to govern the structural dynamics. The electro-elastic model combines the piezoelectric constitutive equations for 3-1 coupling while assuming a uniform electric field. Assuming harmonic response, the following transformation may be derived:³⁷

$$Y_b(x_0 + L_b) = T_{pb}Y_b(x_0),$$
 (3)

where $Y_b(x_0)$ and $Y_b(x_0 + L_b)$ are 4×1 solution vectors of the deformation, shear angle, bending moment, and shear force at each end of the unit cell. T_{pb} is a 4 × 4 transformation matrix whose elements are functions of the unit cell dimensions, material properties, the frequency ω of the incident elastic wave, and the shunt impedance. Applying Bloch-Floquet periodic boundary conditions, Eq. (3) is then cast into an eigenvalue problem³

$$|T_{pb} - e^{ik_x L_b}I| = 0, (4)$$

where k_x is the wavenumber of the incident wave and L_b is the overall length of the unit cell. Solving Eq. (4) yields the wavenumber associated with each incident wave frequency. Comparing the dispersion curves between the open-circuit and LC configurations, the localized phase shift is given by

$$\phi = nL_b (k_{x_{OC}} - k_{x_{LC}}), \tag{5}$$

where ϕ is the local phase shift in radians and n is the number of unit cells that are patterned along the \hat{x} direction. k_{OC} and k_{LC} are the wavenumbers in the open circuit (OC) and LC-shunted configurations. Figure 2 compares the resulting wavenumber, velocity, and phase dispersion curves as a function of incident wave frequency. Each plot contains three dispersion curves, one for the open-circuit and two inductance values ($L_1 = 96 \,\mathrm{mH}$ and $L_2 = 132.5 \,\mathrm{mH}$). The dimensions and material properties for this analysis correspond to the experimental parameters provided in 82 Table I presented in Sec. IV. The curves indicate that a transmission bandgap forms near the local resonance of the unit cell $\frac{6}{4}$ described by Eq. (2). As the frequency of the incident elastic wave $\frac{1}{2}$ approaches this resonance, the wavenumber and propagation speed diverge significantly from the open circuit configuration. The resulting phase shift between the open-circuit and locally resonant

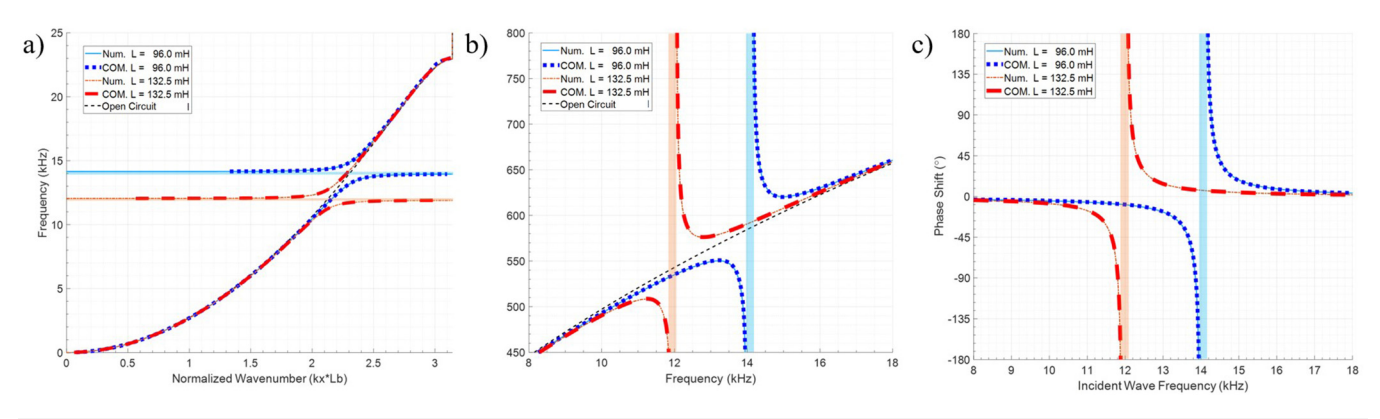


FIG. 2. Numerical and simulated localized dispersion curves for a piezoelectric unit cell with $L=96\,\mathrm{mH}$ ($\sim12\,\mathrm{kHz}$ tuning), $L=132.52\,\mathrm{mH}$ ($\sim14\,\mathrm{kHz}$ tuning), and R = ∞ (open-circuit). (a) Wavenumber dispersion curves, (b) phase velocity dispersion curves, (c) phase dispersion curves. Highlighted region marks the bandgap frequency region.

TABLE I. Experimental parameters.

Dimensions	Beam	Individual unit cell	Piezoelectric layer
Length (mm)	609	15.3	13.1
Width (mm)	9.5	9.5	8.0
Thickness (mm)	2.4	3.4	1.0
Density (kg/m ³)	2700	N/A	7900
Material paramete	ers		
E (GPa)	69.0	N/A	84.0
$d_{31} (V/m)$	N/A	N/A	-155×10^{-12}
$\epsilon_{33}^T/\epsilon_0$ (AU)	N/A	N/A	1600
Circuit parameter	s		
$R_1(k\Omega)$	N/A	3.3	N/A
$R_2(k\Omega)$	N/A	Variable: 2.0-4.0	N/A
$R_3(k\Omega)$	N/A	3.3	N/A
$R_4(k\Omega)$	N/A	1.0	N/A
$C_1(nF)$	N/A	32.0	N/A

cases is reflected in Fig. 2(c). At incident frequencies near the bandgap, large discrete phase shifts can occur. These analytical dispersion curves are verified with corresponding parametric eigenfrequency simulations in COMSOL Multiphysics under the three shunting configurations, as shown in Fig. 2.

III. METASURFACE DESIGN

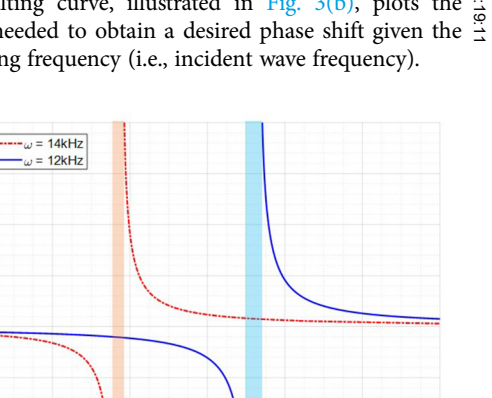
a)

In general, the objective of waveguide design is to modulate incident elastic wavefronts to steer wave propagation in a desired way. Examples include anomalous refraction,³⁸ planar focal lensing,²⁹ and source illusion.³⁹ In this section, the locally resonant unit cell based on piezoelectric LC-shunt (Fig. 1) is extended into a metasurface array and designed to implement anomalous refraction at an arbitrary angle and specified operating frequency. As described by Yu et al., 40 the interaction of a wave with a physical boundary is governed by the Generalized Snell's Law (GSL)

$$k_t \sin(\theta_t) - k_i \sin(\theta_i) = \frac{d\phi}{dy},$$
 (6)

where $k_{i,t}$ are the wavenumbers of the elastic wave in the homogenous medium before and after the interface and $\theta_{i,t}$ are the angles of the incident and transmitted elastic waves, respectively. ϕ is the local phase shift that occurs when the incident wave crosses the interface at any position y. The phase gradient $\frac{d\Phi}{dy}$ describes the change in these phase shifts along the interface. To implement anomalous refraction, the phase gradient must be non-zero and constant and is determined given (1) a known incidence angle and (2) a desired angle of refraction. As illustrated in Fig. 3(a), this phase gradient is discretized among an $m \times n$ array of individual unit cells. Each row in this array is referred to as a "supercell," which itself represents $1 \times n$ array. All subunits in the supercell are tuned to the same resonant frequency, with the overall purpose of implementing a controlled phase shift between the local incident and transmitted wavefields.

To emulate a specified phase gradient, the individual phase shifts across each supercell must be set accordingly. For the metasurface investigated here, this is done by appropriately selecting the inductance values across each supercell. To accomplish this, the analytical procedure described in Sec. II is repeated with some small alterations. The transformation matrix method utilized is small alterations. The transformation matrix method utilized is computationally efficient and flexible, allowing the driving variables to be changed with little to no alteration of the computational procedure. This time, the dispersion curves are computed as a function of inductance value while holding the incident wave frequency constant. The resulting curve, illustrated in Fig. 3(b), plots the inductance values needed to obtain a desired phase shift given the waveguide's operating frequency (i.e., incident wave frequency).



0.12

Inductance (H)

0.14

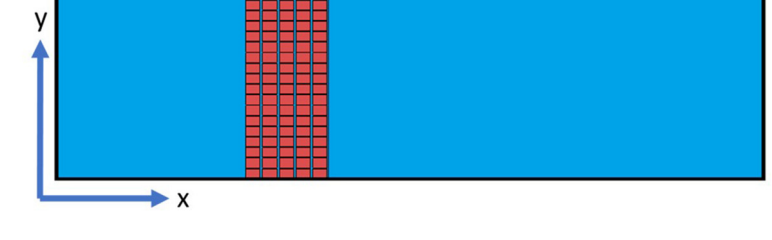


FIG. 3. (a) Top view of the tunable piezoelectric waveguide with m=40 and n=5. A nonzero constant phase gradient results in the refraction of incident waves. (b) Localized phase dispersion plotted as a function of inductance value for both 12 and 14 kHz operating frequencies.

b)

90

-90 -135

-180 L 0.06

0.08

0.1

Phase Shift (°)

0.18

0.16

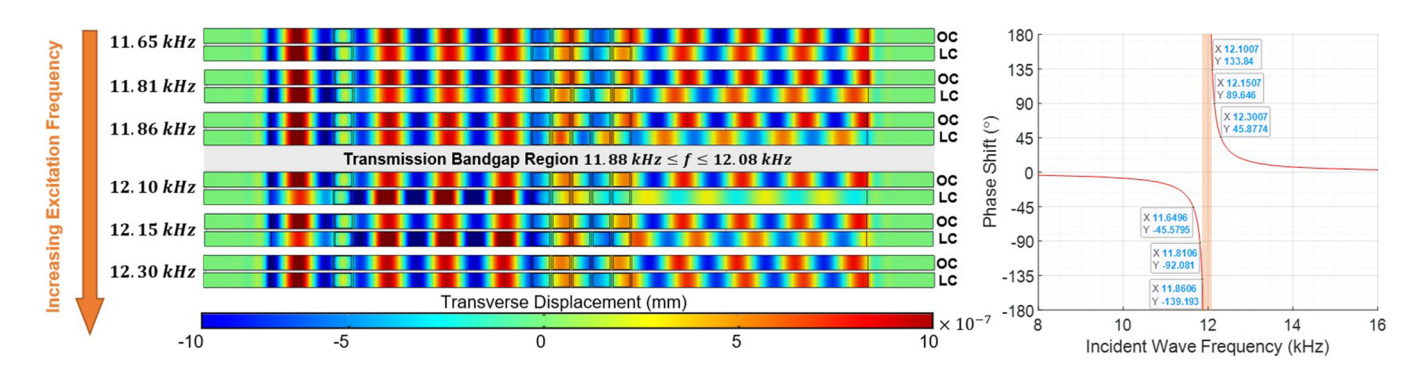


FIG. 4. Verification of localized phase dispersion on an aluminum beam host structure. Left: COMSOL simulations of elastic wave propagation comparing open circuit (OC) and LC-shunted (LC, L = 132.5 mH) configurations with increasing incident wave frequency. Right: Corresponding localized phase dispersion simulation showing the expected phase shift between open-circuit and LC-shunted configurations with a function cell of n=5.

To verify the connection between elastic waveguiding and the theoretical phase analysis, two frequency-domain simulations are performed using COMSOL Multiphysics. Both utilize solid mechanics, electrostatics, electric circuits, and piezoelectric multiphysics modules. The first simulation performs a local phase modulation analysis of a supercell. Incident waves are excited by applying a steady state 1.0 V signal at a specified frequency to the piezoelectric transducer labeled in Fig. 6. In the unimorph configuration, the excitation of this transducer produces a local bending moment in the host structure, leading to the formation and subsequent propagation of quasi-flexural elastic waves. The boundary conditions are set as perfectly matched layers to suppress wave reflections. The phase shift between the open-circuit and LC-shunted configurations on the transmitted wavefield is compared using a contour plot of the vertical beam deflection for various incident wave frequencies. Figure 4 compares the results of this simulation with the phase shift predicted by using the

transformation matrix method. Phase shifts of $\pm 45^{\circ}$, $\pm 90^{\circ}$, and $\pm 135^{\circ}$ are observed at the expected excitation frequencies.

For the second simulation, the phase dispersion analysis is extended to the design of an elastic waveguide based on the GSL.⁴⁰ The metasurface in Fig. 5 is formed with m = 40 supercells each consisting of n = 5 subunits. The excitation is provided by a gaussian load along the left-hand edge, with all edge regions bounded by perfectly matched layers. The resulting Gaussian beam propagates at either 12 or 14 kHz. In Fig. 5(a), a phase gradient of 40.9 rad/m is realized by incrementing the local phase shifts by 22.5° between adjacent supercells. The inductance values needed to realize these increments are selected from the red curve in Fig. 3(b). For this plate configuration and an incident wave frequency of 12 kHz, 88 Eq. (6) predicts a refraction angle of 17.4°, which is approximately observed in the transmitted field. In Fig. 5(b), the inductances are recalibrated for an operating frequency of 14 kHz. This time the phase shifts are incremented by 15° between adjacent supercells,

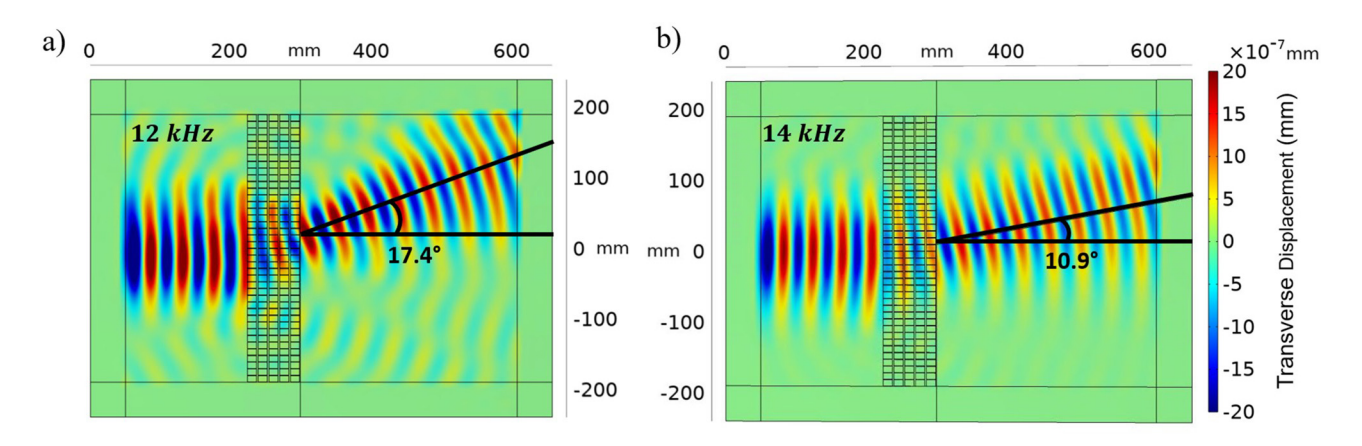


FIG. 5. The transmitted A₀ mode displacement field for two metasurfaces with different incident wave frequencies and phase shift gradients realized by locally resonant LC-shunts. The color bar provided applies to both configurations. (a) f=12 kHz, $\frac{d\theta}{dy}=40.9$ $\frac{\text{rad}}{\text{m}}$ and (b) f=14 kHz, $\frac{d\theta}{dy}=27.3$ $\frac{\text{rad}}{\text{m}}$.

producing a phase gradient of 27.3 rad/m. For this configuration, the GSL predicts a refraction angle of 10.9°. These simulations verify the design process and demonstrate tunability with different angles of refraction and operating frequencies.

IV. EXPERIMENT AND RESULTS

A. Experimental setup

The key to implementing elastic waveguiding via the metasurface is the realization of a controllable phase shift at a local level. This section details an experimental demonstration of elastic phase modulation using a tunable piezoelectric metasurface with synthetic LC-shunts. The tunable phase shifting behavior is demonstrated on a 5 mm thick aluminum beam with n = 5 unit cells, as illustrated in Fig. 6. Both ends of the beam are clamped between sheets of 7000 durometer sorbothane rubber sheets to suppress wave reflections. Sorbothane is a viscoelastic polymer with strain-rate dependent dynamic properties, leading to high hysteretic damping in the acoustic range.⁴¹ As elastic shear waves impinge on this clamped boundary some energy are dissipated in the form heat, reducing the reflected energy. As with the local phase modulation analysis in COMSOL, the actuation PZT is excited by a 1.0 V sinusoid at various frequencies. This voltage is supplied by the onboard generator of a PSV-500-M scanning laser vibrometer front end, enabling the excitations to be precisely triggered with either FFT or time domain measurements of out-of-plane vibration velocity. The dimensions and material properties of this metasurface are provided in Table I.

To realize tunable shunt circuitry, five synthetic inductors are assembled according to Fig. 1(b) using high impedance JFET TL082 operational amplifiers. A $5 \text{ k}\Omega$ potentiometer is used for resistor R2, allowing the synthetic inductance to be analog tuned within a range of 82 mH to ~40 H. Variations in capacitance among samples of piezoelectric material lead to non-uniformity of the local resonances within each supercell if the individual subunits are shunted with the same inductance value. 42 To avoid the

realization of multiple misaligned transmission bandgaps, the inductance values were individually tuned such that the local resonance of each unit cell fell within ± 10 Hz of the two target frequencies (12 and 14 kHz).

For the data acquisition, the configuration in Fig. 6(a) is first used to obtain a 50× spatially averaged frequency response of both the incident and transmitted sides of the metasurface beam. These measurements are illustrated in Fig. 7(a), verifying the presence of a locally resonant bandgap at approximately 12 kHz. The laser vibrometer is then set to measure the time domain response at a single point on the transmitted side of the beam. Steady state responses under open-circuit and LC-shunted configurations are then captured at discrete frequency intervals around the measured bandgap. The raw data are post-processed via a signal correlation approach to eliminate noise and determine the relative phase shift. Figure 7(b) directly compares the filtered time domain responses following amplitude normalization and matched filtering at the specified frequencies.

B. Signal correlation method

When acquiring local phase modulation data, ambient noise presents a significant challenge in validating the performance of an elastic waveguide. It is well established that locally resonant structures produce narrow bandgaps in the transmission of incident When the operating frequency of the waveguide approaches this bandgap region, the signal to noise ratio drops substantially, making it difficult to extract meaningful features of the transmitted wavefield. Traditionally, simple bandpass filtering can be used to reduce noise levels. The relative phase shift can then be determined directly through a comparison of neighboring peaks in the time domain response. This method, however, fails to completely eliminate noise due to the finite bandwidth of the $\frac{30}{4}$ applied filter and is susceptible to transient variations in the $\frac{30}{4}$ ambient noise field. For this reason, a new processing procedure based on signal correlation is adapted to determine the relative

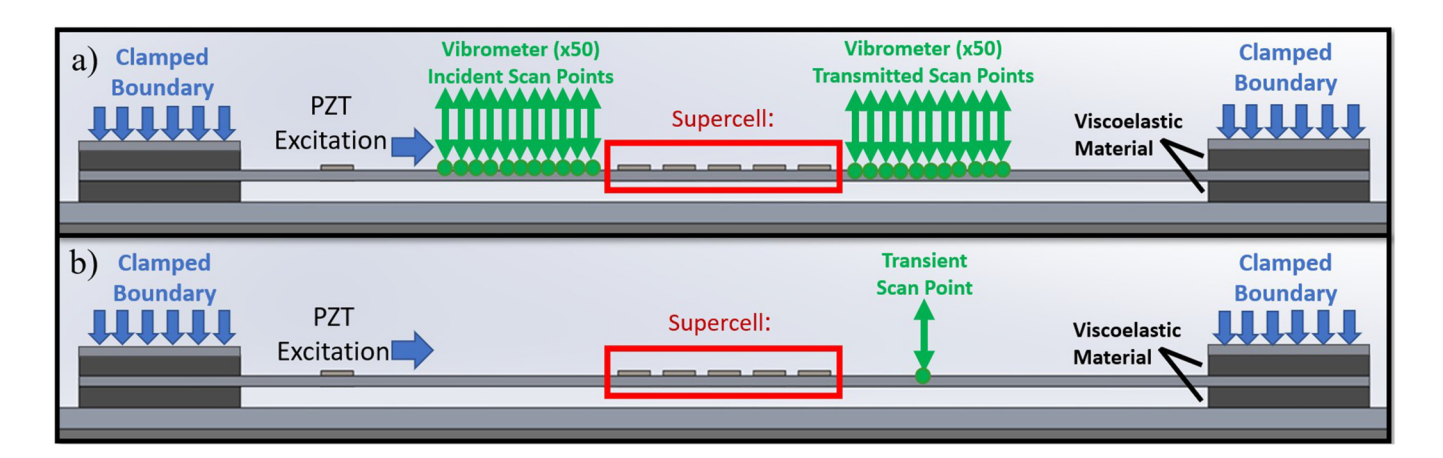


FIG. 6. Side-view diagram of the experimental setup for obtaining (a) frequency-domain (transmission ratio) measurements and (b) time domain phase shift measurements.

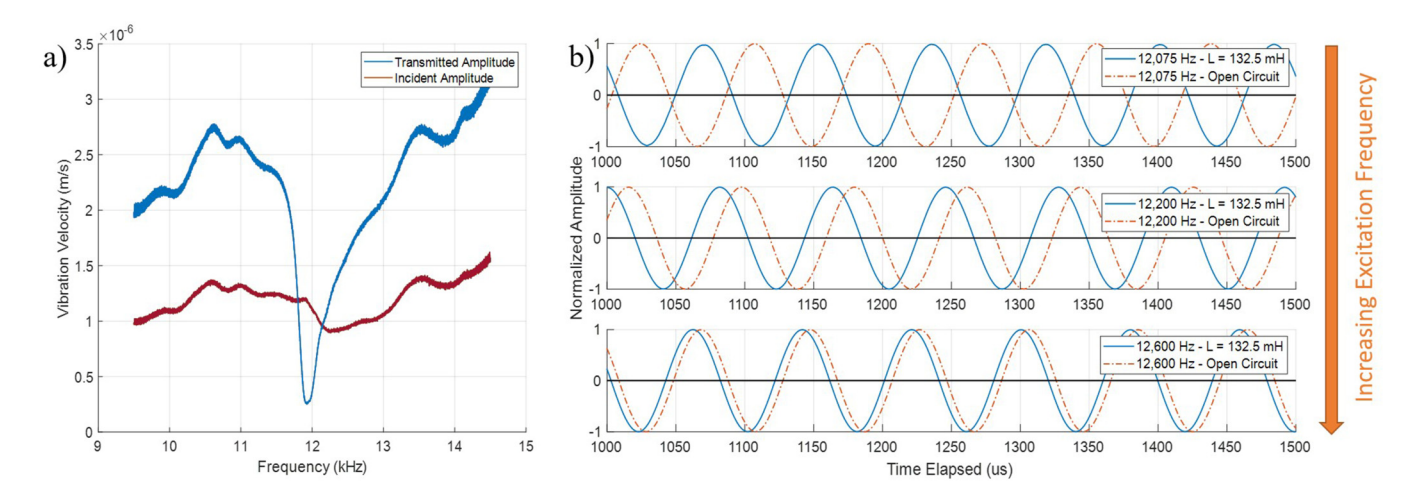


FIG. 7. Vibration velocity measurements obtained with the laser vibrometer. (a) Frequency sweeping excitation for transmission ratio measurement and (b) time domain signal for phase shift measurement after signal correlation processing.

phase between the open circuit and LC-shunted responses. Because the frequency of the incident wave is known *a priori*, matched filtering can be used to simultaneously eliminate noise and extract the relative phase between two transmitted waveforms. ⁴³ In this section, we present a systematic approach to extract the phase shifts produced by the locally resonant piezoelectric unit cell. The correlation between a reference signal and measure response is defined as³²

$$c_n = \frac{1}{T} \int_0^T S_{ref}(\tau) S_{resp}(t - \tau) d\tau, \tag{7}$$

where c_n is the correlation coefficient, $S_{ref}(\tau)$ and $S_{resp}(t-\tau)$ are the reference and measured signals, T is the period, and τ is a time delay that introduces a phase shift. Equation (7) equals zero if $S_{ref}(\tau)$ and $S_{resp}(\tau)$ are uncorrelated, effectively eliminating noise at higher and lower frequencies. Because we defined the phase shift relative to the open-circuit response, it serves as our reference signal $S_{ref}(\tau)$. It is common practice to normalize its amplitude to unity. Due to the lack of a locally resonant bandgap, the measured open-circuit response has a high signal to noise ratio and the normalized reference signal can be approximated as

$$S_{ref}(t) = \sin(\omega t),$$
 (8)

where ω is the frequency of the incident elastic wave. Under the LC-shunted configuration, changes in both phase and amplitude may occur, and noise may be non-negligible within the bandgap region. Thus, the measured LC response is given by

$$S_{resp}(t) = A\sin(\omega t + \alpha) + n(t),$$
 (9)

where *A* is the amplitude of the locally resonant response, α is the phase shift relative to $S_{ref}(t)$, and n(t) represents noise. Multiplying

both sides by orthogonal reference signals, we obtain

$$\sin(\omega t)S_{resp}(t) = A\sin(\omega t + \alpha)\sin(\omega t) + \sin(\omega t)n(t), \tag{10}$$

$$\cos(\omega t)S_{resp}(t) = A\sin(\omega t + \alpha)\cos(\omega t) + \cos(\omega t) n(t), \qquad (11)$$

which are further simplified as

$$\sin(\omega t)S_{resp}(t) = \frac{A}{2}\cos(\alpha) - \frac{A}{2}\cos(2\omega t + \alpha) + \sin(\omega t) \ n(t), \quad (12)$$

$$\cos(\omega t)S_{resp}(t) = \frac{A}{2}\sin(\alpha) + \frac{A}{2}\sin(2\omega t + \alpha) + \cos(\omega t) n(t).$$
 (13)

Notice that the first terms in Eqs. (12) and (13) are time invariant. By applying a lowpass filter with a cutoff frequency less than ω , the time-dependent terms are eliminated and only the DC components $\frac{A}{2}\cos(\alpha)$ and $\frac{A}{2}\sin(\alpha)$ remain. The relative phase shift between the open-circuit and LC responses can then be extracted by taking the arctangent of the ratio of the DC terms. This procedure extracts the phase shift α at the frequency ω only, eliminating noise at all other frequencies. The block diagram for this signal correlation processing is provided in Fig. 8.

Because the arctangent function itself is limited to an output between $\pm 90^\circ$ a simple Boolean operation is performed to add or subtract 180° under the specific convergence conditions of the DC terms. The resulting function correctly outputs the relative phase shift between $\pm 180^\circ$, covering the full range of possible values. It is also worth noting that the DC signals will still contain a single component of noise at the same frequency as the incident wave; however, this noise is generally negligible compared to the measured waveform. This distributed approach offers a significant advantage over a traditional direct comparison of the time domain responses. In addition to eliminating noise through matched

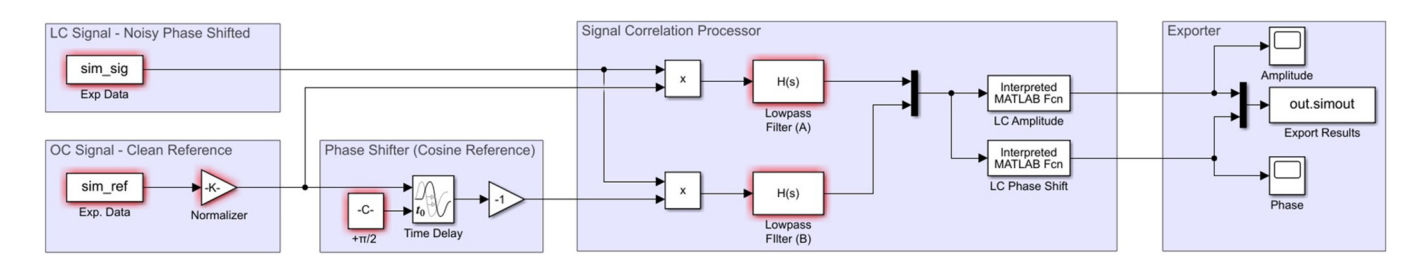


FIG. 8. Simulink block diagram for implementation of signal correlation post-processing.

filtering, it removes human factors and is robust to transient variations in the noise field. With the correct implementation, this method is applicable for either post-processing or real-time acquisition of phase modulation data.

C. Experimental results

This section demonstrates the phase modulation produced by the piezoelectric metasurface with tunable inductive shunts and illustrates the advantages of the signal correlation method over the traditional direct peak comparison method. This comparison is made for both the 12 and 14 kHz tuning configurations by adjusting the R₂ in the synthetic inductance shunts. Figure 9 plots the experimentally measured phase dispersion curves and transmission. The results demonstrate close agreement between the measured phase shifts and the corresponding analytical and finite element models. The measured transmission ratio falls below −3 dB within the ranges of 11.75-12.31 and 13.78-14.23 kHz for each shunt configuration. Within these regions, phase shifts as large as 170° are detected, despite transmission losses in excess of −20 dB.

For excitations very close to the bandgap center frequency, the measured phase dispersion profile diverges from the analytical and finite element models. This behavior is a combined result of two influencing factors: sensitivity and damping. High sensitivity in the phase shifts to the excitation frequency and slight misalignment of the inductive shunts in each supercell. Slight variations among the individually tuned synthetic inductors result in nonuniformity of the local resonances between adjacent unit cells. The resulting shifts in the overall phase profile result in high uncertainty in the experimental results within this sensitive region. To reduce this uncertainty two approaches can be taken. The first is to tune the resonances of adjacent unit cells with higher precision. The second is to increase the bandgap width. Yi and Collet 44 explored how the addition of a negative capacitance branch to a locally resonant unit cell increases the electromechanical coupling and broadens the bandgap width. While specific details are beyond the scope of the present work, increasing bandgap width generally reduces the sensitivity of realized phase shifts to the tuning parameter.

Resistive damping may also play a role in the phase modulation results, especially in the vicinity of the transmission $\frac{3}{2}$

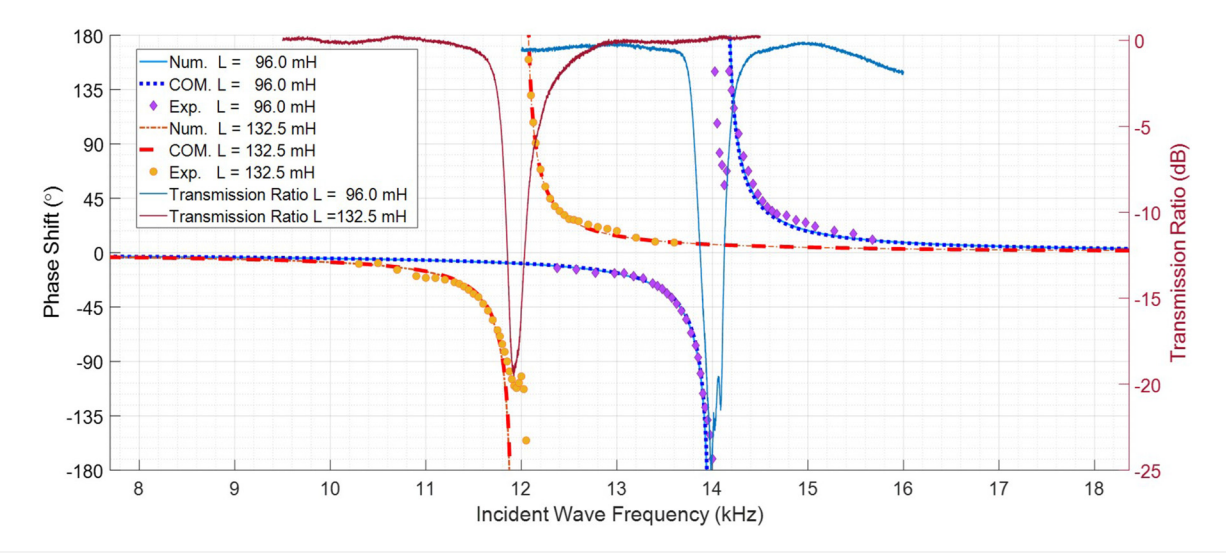


FIG. 9. Results of localized phase dispersion measurement of the LC-shunted piezoelectric metasurface beam tuned to 12 and 14 kHz, respectively (left vertical axis). Overlayed is the transmission ratio measured by comparing the amplitude of incident and transmitted waves (right vertical axis).

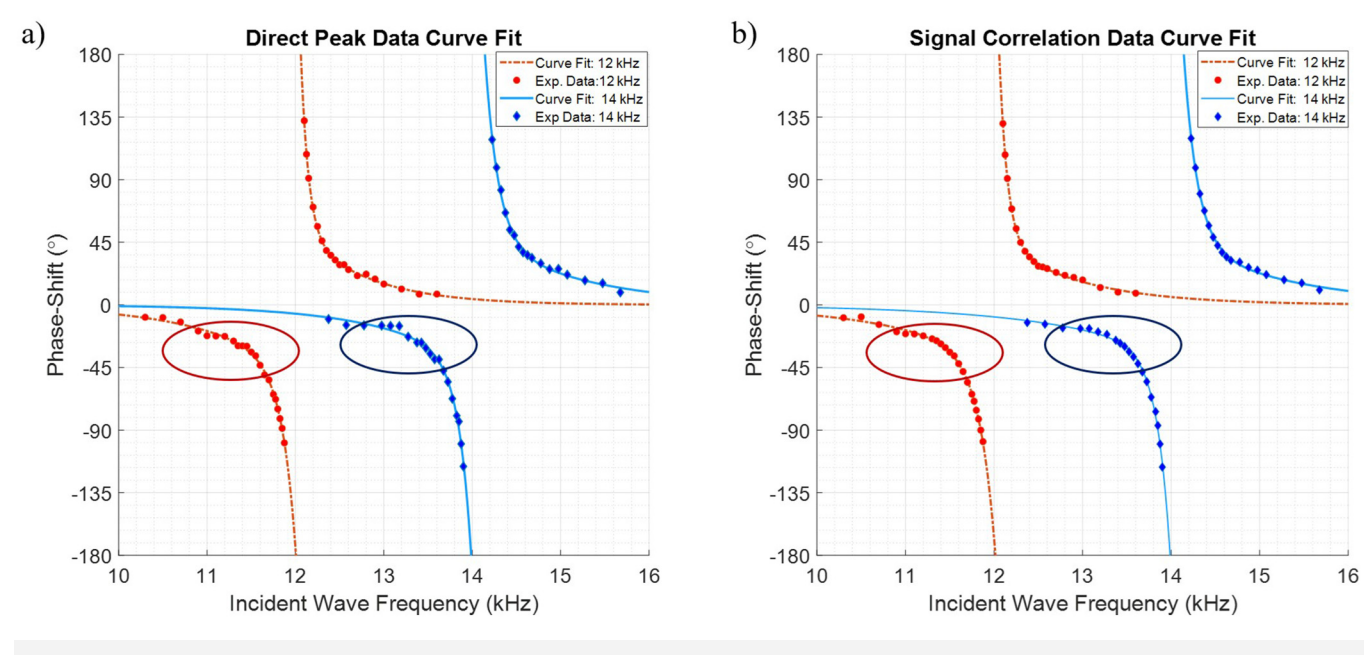


FIG. 10. Comparison of phase dispersion measurement via (a) a manual approach of direct peak comparison of open circuit and LC-shunted time domain signals and (b) signal correlation processing.

bandgap.³² Within this region, the incident waves excite the electrical LC-oscillators close to their resonant frequencies, exciting large currents within the unit cell circuitry. Because energy dissipation is proportional to the square of electrical current $(P = I^2R)$, the resistive damping may indeed affect the realized phase shifting. In the recent literature, Jian *et al.*²² drew to attention the significant attenuation of an LC-shunt's resonant peak when applied with a resistance of 200 Ω . In this research, upon measurement using LCR meter we identified the resistance value was approximately 12 Ω across the unit cell circuit. In the derivation of Eq. (2), the ideal $\frac{1}{2}$

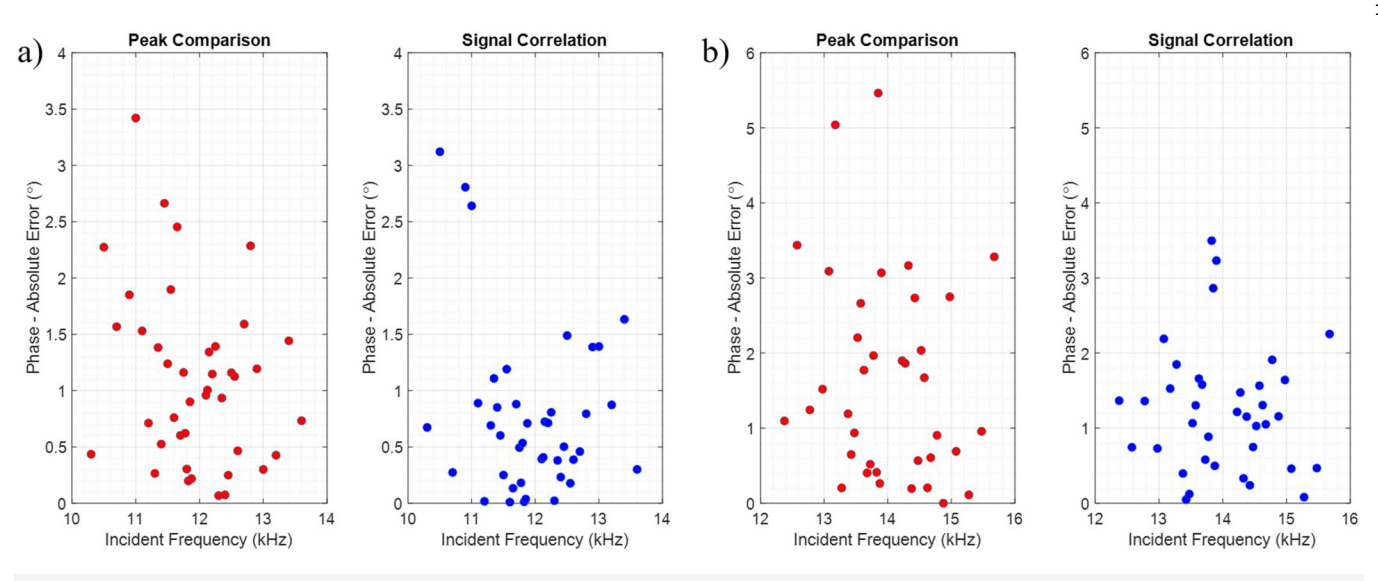


FIG. 11. Assessment of phase dispersion measurement via direct peak comparison of time domain signals to signal correlation processing. (a) Results for the 12 kHz bandgap experimental case study and (b) 14 kHz case study.

operational amplifier assumptions of virtual short and infinite input impedance lead to a purely reactive element with no real resistance. With the small resistance in the experimental setup, these assumptions appear to be reasonable. Indeed, as illustrated in Fig. 9, the theoretical predictions offer a good approximation of the experimentally measured results for most excitation frequencies. Influences of larger resistances and other mistuning factors will be subject to future research.

To evaluate the advantages of the signal correlation processing for the phase measurement, the approach is compared to the direct peak comparison method. Figure 10 illustrates the phase dispersion profiles obtained using each method, with outliers removed and the data fit to a least square exponential regression. For the direct peak comparison, the raw time domain responses are fed through a bandpass filter and normalized to unity. The open-circuit and LC-shunted responses are then visually compared, and the phase is measured directly from the time-delay cursors between adjacent peaks. For the signal correlation processing, the procedure previously detailed is used with a cutoff frequency of 300 Hz for the lowpass filters. Because the ambient level is low and filtered in both instances, the differences in the phase shift measurements obtained are subtle. Figure 11 plots the error between each dataset and the corresponding curve fit. Figures 11(a) and 11(b) demonstrate a 30% and 25% reduction in random error when using signal correlation processing over direct peak comparison. This improvement is primarily the result of the signal correlation procedure, restricting the noise to the excitation frequency. The traditional method with bandpass filtering permits a broader band of noise in the acquired

Overall, these results demonstrate the tunability and phase shifting capability of the locally resonant piezoelectric unit cell. Moreover, the application of signal correlation processing eliminates the need for human involvement in phase measurements and improves the precision of the data collection. The proposed method of validating localized phase dispersion of a supercell offers a systematic approach applicable to post-processing or real-time acquisition of time domain measurements. This approach could be widely extended to experimentally investigate the performance of metasurfaces for elastic waveguiding.

V. CONCLUSIONS

This research presents the experimental investigation of a tunable, locally resonant piezoelectric metasurface for waveguiding applications. The acquisition of phase delay measurements is enhanced with matched filtering, taking advantage of the correlation between the incident and transmitted waveforms to eliminate ambient noise and determine phase. The fundamental operating principle for phase gradient metasurfaces is to realize discrete, localized phase shifts that are tailored to control the propagation of incident waves according to the generalized Snell's law. By analyzing the localized phase dispersion produced by a handful of unit cells, it is shown that a metasurface can be designed to implement anomalous refraction at a specified angle over a wide range of individual frequencies. This work demonstrates that phase shifts as large as 170° can be obtained using a piezoelectric supercell with tunable shunt circuitry. The metasurface is configured to operate

with bandgaps at 12 and 14 kHz, demonstrating online tunability of the phase dispersion profile. Using the proposed signal correlation processing, phase delay measurement can be acquired in either post-processing or real-time with high precision. It is hoped that this approach will be utilized by the research community to experimentally validate the phase shifting behavior of future phase gradient metasurfaces.

ACKNOWLEDGMENTS

This research is supported, in part, by NSF under Grant Nos. 2136520 (GRFP) and 1825324.

AUTHOR DECLARATIONS

Conflict of Interest

The authors have no conflicts of interest to disclose.

Author Contributions

Joshua Dupont: Conceptualization (equal); Data curation (lead); Formal analysis (equal); Investigation (lead); Methodology (equal); Resources (supporting); Software (lead); Validation (lead); Visualization (lead); Writing - original draft (lead); Writing review & editing (equal). Ting Wang: Data curation (supporting); Formal analysis (equal); Investigation (supporting); Writing review & editing (supporting). Richard Christenson: Project administration (equal); Resources (equal); Supervision (supportadministration (equal); Resources (equal); Supervision (supporting). Jiong Tang: Conceptualization (equal); Formal analysis (supporting); Funding acquisition (equal); Methodology (equal); Project administration (lead); Resources (equal); Supervision (lead); Visualization (supporting); Writing – review & editing (equal).

The data that support the findings of this study are available from the corresponding author upon reasonable request.

REFERENCES

- ¹J. H. Oh, H. Min Seung, and Y. Young Kim, Appl. Phys. Lett. 104(7), 073503 (2014).
- ²J. Guo, C. Yang, Q. Dai, and L. Kong, Sensors 19(17), 3771 (2019).
- ³C. Wu, X. Liu, and Y. Ying, ACS Sensors **6**(4), 1446–1460 (2021).
- ⁴L. Yu, Z. Tian, X. Li, R. Zhu, and G. Huang, J. Intell. Mater. Syst. Struct. 30(9), 1306-1317 (2019).
- ⁵Y. Y. Chen, R. Zhu, M. V. Barnhart, and G. L. Huang, Sci. Rep. 6, 35048 (2016).
- ⁶H. Zhu, T. F. Walsh, and F. Semperlotti, Appl. Phys. Lett. 113, 221903 (2018).
- ⁷P. Dorin and K. W. Wang, Front. Mater. 7, 602996 (2021).
- ⁸M. Alshaqaq and A. Erturk, IOP Smart Mater. Struct. 30, 015029 (2021).
- ⁹Z. Lin, H. A. Ba'ba'a, and S. Tol, IOP Smart Mater. Struct. **30**, 075037 (2021).
- ¹⁰Z. Lin and S. Tol, J. Vib. Acoust. **143**(6), 061005 (2021).
- ¹¹H. Zhu and F. Semperlotti, Phys. Rev. Lett. 117, 34302 (2016).
- 12 L. Cao, Z. Yang, and Y. Xu, J. Sound Vib. 418, 1–14 (2018).
- 13 A. L. Chen, S. S. Yuan, Y. F. Wang, H. T. Zhou, and Y. S. Wang, ASME Appl. Mech. Rev. 74, 020801 (2022).
- ¹⁴V. C. De Sousa, C. Sugino, C. De Marqui, and A. Erturk, J. Appl. Phys. 124,
- ¹⁵V. C. De Sousa, D. Tan, C. De Marqui, and A. Erturk, Appl. Phys. Lett. 113,

- ¹⁶R. K. Messenger, Q. T. Aten, T. W. McLain, and L. L. Howell, J. Microelectromech. Syst. 18, 1267 (2009).
- ¹⁷X. Shi, Y. Zhu, X. Fan, H. Wu, P. Wu, X. Ji, Y. Chen, and J. Liang, Matter 5(5), 1547–1562 (2022).
- ¹⁸S. Yuan, A. L. Chen, and Y. S. Wang, J. Sound Vib. **470**, 115168 (2020).
- 19X. Li, Y. Chen, G. Hu, and G. Huang, IOP Smart Mater. Struct. 27, 045015 (2018).
- ²⁰T. Ma, Y. Chen, H. Chen, Y. Zheng, G. Huang, J. Wang, and J. Du, J. Sound Vib. 491, 115738 (2021).
- ²¹Y. Jian, L. Tang, G. Hu, Z. Li, and K. C. Aw, Int. J. Mech. Sci. 218, 107068 (2022).
- ²²Y. Jian, G. Hu, L. Tang, W. Tang, M. Abdi, and K. C. Aw, Eng. Struct. 275, 115091 (2023).
- ²³O. Alfahmi, C. Sugino, and A. Erturk, IOP Smart Mater. Struct. 31, 095044 (2022).
- ²⁴T. M. P. Silva, M. A. Clementino, V. C. de Sousa, and C. De Marqui, IEEE/ ASME Trans. Mech. 25, 1076 (2020).
- ²⁵G. Hu, A. C. M. Austin, V. Sorokin, and L. Tang, Mech. Syst. Signal Proc. 146, 106982 (2021).
- ²⁶C. Sugino, M. Ruzzene, and A. Erturk, Phys. Rev. Appl. 13, 061001 (2020).
- ²⁷X. Li, Y. Chen, X. Zhang, and G. Huang, Extr. Mech. Lett. **39**, 100837 (2020).
- ²⁸Y. Jian, L. Tang, G. Hu, Y. Wang, and K. C. Aw, IOP Smart Mater. Struct. 31, 075026 (2022).
- ²⁹Z. Lin and S. Tol, J. Phys. D: Appl. Phys. **56**, 164001 (2023).
- ³⁰G. Hu, J. Xu, L. Tang, C. Lan, and R. Das, J. Intell. Mater. Syst. Struct. 31(3), 389–407 (2020).

- 31Y. Zheng, J. Zhang, Y. Qu, and G. Meng, J. Sound Vib. 503, 116113 (2021).
- ³²X. Zhang, R. Yan, and J. Xu, J. Appl. Phys. **128**, 174903 (2020).
- ³³K. W. Wang and J. Tang, Adaptive Structural Systems with Piezoelectric Transducer Circuitry (Springer, 2008), ISBN:978-1588298218.
- ³⁴M. Vatavu, F. Turcu, and V. Nastasescu, J. Appl. Sci. 9, 4777 (2019).
- 35C. Sugino, M. Ruzzene, and A. Erturk, IEEE/ASME Trans. Mech. 23(5), 2144–2155 (2018).
- 36Y. Chen, J. Hu, and G. Huang, J. Intell. Mater. Syst. Struct. 27, 1337–1347 (2016).
- 37S. Li, Ph.D. dissertation, University of Connecticut (2019).
- ³⁸S. Li, J. Xu, and J. Tang, Appl. Phys. Lett. **112**, 021903 (2018).
- ³⁹Y. Liu, Z. Liang, F. Liu, O. Diba, A. Lamb, and J. Li, Phys. Rev. Lett. 119, 34301 (2017).
- ⁴⁰N. Yu, P. Genevet, M. A. Kats, F. Aieta, J. P. Tetienne, F. Capasso, and Z. Gaburro, Science **334**(6054), 333–337 (2011).
- ⁴¹K. Dwivedi, S. Das, and S. G. Rajasekharan, "Experimental and numerical investigation on effects of viscoelastic rubber and local resonator mass on broadband vibration attenuation in acoustic-metamaterial plates," J. Intell. Mater. Syst. Struct. (published online) (2023).
- ⁴²N. Elvin, A. Elvin, and B. Z. Senderos, J. Intell. Mater. Syst. Struct. **29**(5), 816–829 (2018).
- ⁴³B. P. Lathi, Signal Processing and Linear Systems (Oxford University Press, 1998), ISBN:9780195219173.
- 44K. Yi and M. Collet, J. Sound Vib. 493, 115837 (2021).